AIAA JOURNAL
Vol. 48, No. 7, July 2010

Large-Eddy/Reynolds-Averaged Navier–Stokes Simulations of Sonic Injection into Mach 2 Crossflow

John A. Boles* and Jack R. Edwards†
North Carolina State University, Raleigh, North Carolina 27695
and
Robert A. Baurle‡
NASA Langley Research Center, Hampton, Virginia 23681

DOI: 10.2514/1.J050066

Computational predictions of transverse injection of air, helium, and ethylene into a Mach 1.98 crossflow of air are presented. A hybrid large-eddy simulation/Reynolds-averaged Navier–Stokes turbulence model is used. A blending function, dependent on modeled turbulence variables, is used to shift the turbulence closure from the Menter k-ω model near solid surfaces to a Smagorinsky subgrid model in the outer part of the incoming boundary layer and in the jet mixing zone. The results show reasonably good agreement with time-averaged Mie-scattering images of the plume structure for both helium and air injection and with experimental surface pressure distributions, even though the penetration of the jet into the crossflow is slightly overpredicted. Predictions of ethylene mole fraction at several transverse stations within the plume are in good agreement with time-averaged Raman-scattering mole-fraction data. The model results are used to examine the validity of the commonly used assumption of the constant turbulent Schmidt number in the intense mixing zone downstream of the injection location. The assumption of a constant turbulent Schmidt is shown to be inadequate for jet mixing dominated by large-scale entrainment.

Nomenclature

C	=	logarithmic-law wall intercept
C_S	=	Smagorinsky constant
C_μ	=	turbulence model constant
D	=	injector diameter, m
d	=	distance to nearest wall, m
d_w^+	=	wall coordinate based on wall kinematic viscosity
d^+	=	wall coordinate based on local kinematic viscosity
J	=	momentum-flux ratio
k	=	turbulence kinetic energy, m^2/s^2
r	=	injector radius, m
S	=	strain rate, s^{-1}
T	=	temperature, K
u, v, w	=	velocity in x, y, and z directions, m/s
u_{vd}	=	van Driest-transformed velocity, m/s
u_τ	=	friction velocity, m/s
x, y, z	=	streamwise, bottom-wall normal, and spanwise direction distances in Cartesian coordinates, m
α_1	=	model constant
Γ	=	hybrid model blending function
Δ	=	filter width, cell size, m
δ	=	boundary-layer thickness, m
η	=	ratio of turbulent length scales
κ	=	von Karman constant
λ	=	Taylor microscale
μ_t	=	eddy viscosity, kg/(m · s)
Π	=	Coles wake parameter
ρ	=	density, kg/m^3
ρ_s	=	species density, kg/m^3
υ_t	=	kinematic eddy viscosity, m^2/s
υ_w	=	wall kinematic viscosity, m^2/s
$\upsilon_{t,\mathrm{sgs}}$	=	Smagorinsky subgrid kinematic eddy viscosity, m^2/s
φ	=	turbulence model constant
ω	=	turbulence frequency, s^{-1}

Received 14 July 2009; revision received 7 December 2009; accepted for publication 18 December 2009. Copyright © 2010 by John A. Boles. Published by the American Institute of Aeronautics and Astronautics, Inc., with permission. Copies of this paper may be made for personal or internal use, on condition that the copier pay the $10.00 per-copy fee to the Copyright Clearance Center, Inc., 222 Rosewood Drive, Danvers, MA 01923; include the code 0001-1452/10 and $10.00 in correspondence with the CCC.

*Research Assistant, Department of Mechanical and Aerospace Engineering. Student Member AIAA.
†Professor, Department of Mechanical and Aerospace Engineering. Associate Fellow AIAA.
‡Aerospace Engineer, Hypersonic Air Breathing Propulsion Branch. Associate Fellow AIAA.

I. Introduction

UNDERSTANDING the flow physics involved with sonic injection into a supersonic crossflow plays a vital role in the analysis and design of supersonic combustive ramjet (scramjet) engines. In a scramjet combustor, it is critical that the injected fuel be sufficiently mixed with the oxidizer so that combustion may occur. Achieving adequate mixing within a scramjet combustor is nontrivial, since the flow residence time in these devices is often comparable to the chemical time scales. As a result, studying the impact of using different fuels and injection schemes is vitally important to further advance the design of combustors for air-breathing hypersonic flight. Unfortunately, experimental studies of these complex flows are costly to perform, and reliable measurements are often difficult to obtain, forcing an increased reliance on computational studies to augment the databases of sonic injection into supersonic flowfields.

Figure 1 shows the flowfield features that result from transverse injection into a supersonic crossflow. Optical methods [1–7] allowed researchers to discern the major flow phenomena, such as the prominent bow shock, the Mach disk in the interior of the injection plume, the counter-rotating vortices in the injection plume, and the wake and vortex regions beneath the injection plume. More recent studies [8–14] have used laser diagnostics in addition to optical techniques and gas-sampling methods to glean more information from wind-tunnel tests. Even with newer technology, quantitative results are often limited.

Computational studies can also offer insight into the mechanics of these flows. Reynolds-averaged Navier–Stokes (RANS) predictions using a variety of turbulence models have been obtained by Uenishi et al. [15], Tam et al. [16], Palekar et al. [17], Maddalena et al. [18], and Manna and Chakraborty [19], among others. In general, few studies using standard turbulence models have been able to successfully predict the plume structure and the jet penetration rate, although results do tend to improve with mesh refinement.

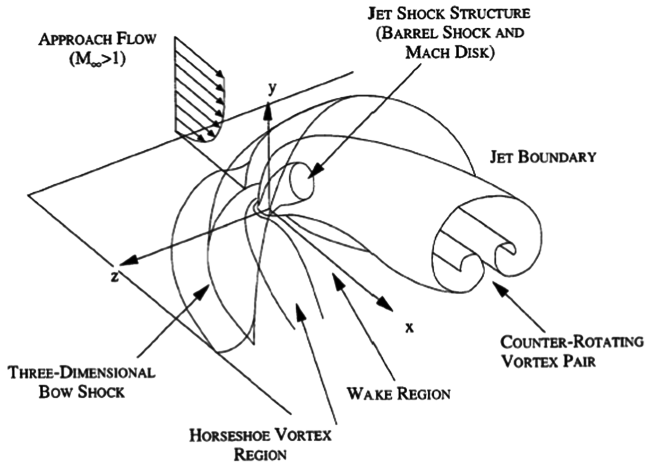

Fig. 1 Perspective view of transverse flowfield [10].

More recent RANS studies [20–22] have incorporated variable Schmidt/Prandtl number effects and have achieved a generally better agreement with experimental data.

Large-eddy-simulation (LES) and detached-eddy-simulation (DES) techniques [23,24] have also been used to predict sonic-injection flowfields. Kawai and Lele [25] conducted an LES of sonic injection into a supersonic crossflow, using the experiment of Santiago and Dutton [26] as a reference point. To reduce the expense of the calculations, the Reynolds number was lowered by a factor of six, relative to the experiment, and a laminar inflow boundary layer was assumed. DES techniques have been used to predict the structure of sonic-injection flowfields by Peterson et al. [27] and Higgins and Schmidt [28]. In these calculations, the experimental conditions are properly matched. Varying levels of predictive capability have been achieved, dependent on the level of mesh refinement, the DES model variant, and the inflow boundary condition treatment; but, in general, the DES results provide an improvement over RANS calculations.

In the present work, a hybrid LES/RANS method [29,30] is used to simulate some of the experiments of Gruber et al. [10–13], which involve the injection of sonic air or helium into a Mach 1.98 air crossflow, and the experiments of Lin et al. [14], which involve sonic injection of ethylene into a Mach 1.98 air crossflow. This study is part of a continuing effort to develop hybrid LES/RANS strategies that are more suited for computing strongly interacting, three-dimensional wall-bounded flows encountered in high-speed engine concepts. The viewpoint adopted in this work is that the RANS component functions as a type of near-wall turbulence closure, with the shift from RANS to LES governed by a flow-dependent blending function that is designed to transition (in a time-averaged sense) from RANS to LES near the edge of the logarithmic region of the boundary layer. The model differs from conventional DES in this regard. Recycling/rescaling techniques are used to initiate and sustain large-eddy structures at inflow boundaries. The remainder of this paper describes the turbulence closure models used, the numerical methods, the initialization procedure, and the results of the investigation.

II. Numerical Model

A. Governing Equations and Turbulence Model

The Favre-filtered Navier–Stokes equations, expanded to include separate transport equations for individual species, are solved in a finite-volume form in this study. The interpretation of the averaging process in a general sense leads to a similarity between the Favre-filtered form used in LES and the Favre-averaged form used in unsteady RANS modeling. As such, the same set of equations can be solved in a time-dependent manner, and the shift between an LES interpretation and an unsteady RANS interpretation depends on the form of the model for the unresolved stress, diffusion, and conduction terms. In this study, a simple approach based on Boussinesq/gradient-diffusion assumptions is used to facilitate this shift. Constant values for the turbulent Schmidt and Prandtl numbers (0.9 and 0.9) are assumed for species diffusion and heat conduction. With these assumptions, the closure problem reduces to specifying the eddy viscosity.

The hybrid LES/RANS model used in this investigation [29,30] is based on Menter's k-ω/k-ε baseline (BSL) model [31] and only involves modifications to the eddy-viscosity description:

$$\mu_t = \rho\nu_t = \rho\left[\Gamma\frac{k}{\omega} + (1-\Gamma)\nu_{t,\mathrm{sgs}}\right] \tag{1}$$

As the blending function Γ approaches one, the closure approaches its RANS description, and as it approaches zero, a subgrid eddy viscosity is obtained. This work uses a Smagorinsky model for the subgrid viscosity, defined as

$$\nu_{t,\mathrm{sgs}} = C_s\Delta^2 S; \qquad C_s = 0.01; \qquad \Delta = (\Delta_x\Delta_y\Delta_z)^{1/3}$$
$$S = \left[\frac{\partial\tilde{u}_i}{\partial x_j}\frac{\partial\tilde{u}_j}{\partial x_i} + \frac{\partial\tilde{u}_i}{\partial x_j}\frac{\partial\tilde{u}_i}{\partial x_j} - \frac{2}{3}\left(\frac{\partial\tilde{u}_i}{\partial x_i}\right)^2\right]^{1/2} \tag{2}$$

The blending function Γ is based on the ratio of the wall distance d to a modeled form of the Taylor microscale:

$$\Gamma = \frac{1}{2}\left(1 - \tanh\left[5\left(\frac{\kappa}{\sqrt{C_\mu}}\eta^2 - 1\right) - \phi\right]\right); \qquad \eta = \frac{\mathrm{d}}{\alpha_1\lambda} \tag{3}$$

where the Taylor microscale is defined as $\lambda = \sqrt{\nu/C_\mu\omega}$, and ϕ is set to $\tanh^{-1}(0.98)$ in order to fix the balancing position (i.e., where $(\kappa/\sqrt{C_\mu})\eta^2 = 1$) to $\Gamma = 0.99$. The constant α_1 is chosen to force the average LES to RANS transition position ($\Gamma = 0.99$) for equilibrium boundary layers to occur at the point where the wake law starts to deviate from the log law. To determine α_1 for a particular inflow boundary layer, the procedure taken from [29] is used. First, a prediction of the equilibrium boundary layer is obtained (given freestream properties, a specified wall thermal condition, and a value for the boundary-layer thickness) from Coles's law of the wall/wake, along with the van Driest transformation:

$$\frac{u_{\mathrm{vd}}}{u_\tau} = \frac{1}{\kappa}\ell_n(d_w^+) + C + 2\frac{\Pi}{\kappa}\sin^2\left(\frac{\pi}{2}\frac{\mathrm{d}}{\delta}\right); \qquad d_w^+ = \frac{u_\tau d}{\nu_w} \tag{4}$$

An initial estimate for the outer extent of the log layer is defined by finding the value of d_w^+, such that

$$\left[\frac{1}{\kappa}\ell_n(d_w^+) + C\right]\Big/\left(\frac{u_{\mathrm{vd}}}{u_\tau}\right) = 0.98$$

The value of $d^+ = u_\tau d/\nu$ that corresponds to this value of d_w^+ is then found through the use of Walz's formula [32] for the static temperature distribution within the boundary layer. The model constant is then obtained by the equivalence $d^+ = \alpha_1^2$, which arises from the use of inner-layer scaling arguments for k and ω. For the inflow boundary layers in the helium and air cases (Tables 1 and 2), a value of $\alpha_1 = 37.56$ was calculated. A lower value of $\alpha_1 = 34.24$ was calculated for the ethylene injection case (Table 3), as the Reynolds number per meter is smaller. A recycling/rescaling procedure [29], applied to the fluctuating fields, is used to sustain grid-resolved turbulent structures in the outer part of the incoming boundary layer.

B. Numerical Methods

A planar relaxation subiteration procedure coupled with a Crank–Nicholson time discretization is used to advance the governing equations at second-order temporal accuracy. Inviscid fluxes are calculated using Edwards' low-diffusion flux-splitting upwind scheme [33]. These fluxes are extended to second-order accuracy, using the piecewise parabolic method [34]. The reconstruction procedures are applied to the primitive-variable vector $V = [p_s, u, v, w, T, k, \omega]$, where p_s is the species partial pressure. The code used to perform the simulations has been parallelized using

Table 1 Air injection case: freestream and injectant properties

Conditions	Values
Wind-tunnel total temperature	302 K
Wind-tunnel total pressure	317 kPa
Mach number	1.98
Boundary-layer thickness (δ)	6.35 mm
Injectant total temperature	300 K
Injectant total pressure	902 kPa
Injectant exit Mach number	1.0
Injector diameter	6.35 mm
Momentum-flux ratio (J)	2.90

Table 2 Helium injection case: freestream and injectant properties

Parameters	Values
Wind-tunnel total temperature	300 K
Wind-tunnel total pressure	317 kPa
Mach number	1.98
Boundary-layer thickness (δ)	6.35 mm
Injectant total temperature	300 K
Injectant total pressure	832 kPa
Injectant exit Mach number	1.0
Injector diameter	6.35 mm
Momentum-flux ratio (J)	2.93

Table 3 Ethylene injection case: freestream and injectant properties

Parameters	Values
Wind-tunnel total temperature	300 K
Wind-tunnel total pressure	241 kPa
Mach number	2.0
Boundary-layer thickness (δ)	6.35 mm
Injectant total temperature	315 K
Injectant total pressure	127.5 kPa
Injectant exit Mach number	1.0
Injector diameter	4.762 mm
Momentum-flux ratio (J)	0.5

three-dimensional spatial domain decomposition with the message-passing interface libraries used for communication between processors.

C. Initial Condition and Time Advancement Details

To provide an initial condition for the incoming boundary layer, a two-dimensional RANS simulation was performed for the facility nozzle [35]. A three-dimensional mesh with clustering to the injector location and to the walls was then generated. For the air and helium injection cases, the mesh extends $+/-12$ injector diameters in the streamwise (x) direction, $+/-6$ injector diameters in the spanwise (z) direction, and 16 injector diameters in the transverse (y) direction. A metric of approximately 15 cells/incoming boundary-layer thickness was used in the isotropic (x and z) directions and in the y region traversed by the jet plume, leading to about 11.8 million cells. The mesh was clustered to the plate surface and to the injector location; thus, the resolution near the injector is finer than the 15 cells/boundary-layer thickness metric used for the boundary layer of the approach flow. About 625 cells were located over the x-z region occupied by the circular injector port. For the ethylene injection case, the mesh extends 15 injector diameters upstream of the injector and 25.5 injector diameters downstream of the injector, and $+/-6$ injector diameters in the spanwise direction and 15 injector diameters in transverse direction. The grid is longer in the streamwise direction for this case than for the simulations of the Gruber et al. experiments [10–13] so as to include the $x/D = 25.3$ plane, where Lin et al. [14] provided a Raman-scattering mixture fraction data. For the ethylene injection case, an x and z spacing of 20 cells/jet diameter (which is approximately 19 cells/incoming boundary-layer thickness) was used for the domain near the injection plume, with the spacing expanding to 15 cells/jet diameter upstream of the injector and on the edges of the domain in the spanwise direction, yielding approximately 19.96 million cells. About 330 cells were located over the x-z region occupied by the circular injector port for the ethylene injection case. The exit conditions for the injectants were obtained by computing the axisymmetric flow within the injector nozzle. These solutions were then interpolated to the ghost cells associated with the injector port, with no attempt made to match the mesh topologies or to use time-dependent forcing of the jet fluid.

Periodic boundary conditions were applied in the z-direction upstream of the injector, and extrapolation conditions were used at the upper extent of the domain in the y direction, at the downstream end in the x direction, and downstream of the injector in the z direction. The simulations therefore correspond to injection into an unbounded domain in the y and z planes, and possible blockage effects caused by boundary-layer growth on the side and upper walls of the test section are not accounted for. These concessions may affect the predictions of jet penetration, as discussed later. A Menter-BSL RANS solution with injection was then obtained and used as the initial condition for the LES/RANS simulations. The time-dependent calculations were simulated for approximately five flow-through times in order to remove startup transients; then, statistics were collected for approximately 7 ms of physical time ($\sim$24 flow-through times, based on the freestream conditions and domain length) at a time step of 0.25 μs.

III. Results and Discussion

A. Inflow Boundary Layer

Freestream conditions and injector conditions for the three cases are provided in Tables 1–3. Velocity and Reynolds shear-stress profiles as calculated by the LES/RANS formulation for the ethylene injection case are shown in Fig. 2. The velocity profiles are normalized by the freestream velocity (519 m/s), and the y coordinate is normalized by the target boundary-layer thickness (0.00635 m). The Reynolds shear-stress profiles (resolved and modeled) are normalized by the wall value of the shear stress [36,37]. The results are compared with normalized data from a zero-pressure-gradient boundary-layer experiment at a similar Reynolds number [36]. Good agreement with the experimental velocity profile is indicated, but the predicted Reynolds-stress values are less than shown in the experiment. This may imply that the boundary layer has yet to recover fully from the favorable pressure gradient experienced in the divergent part of the wind-tunnel nozzle.

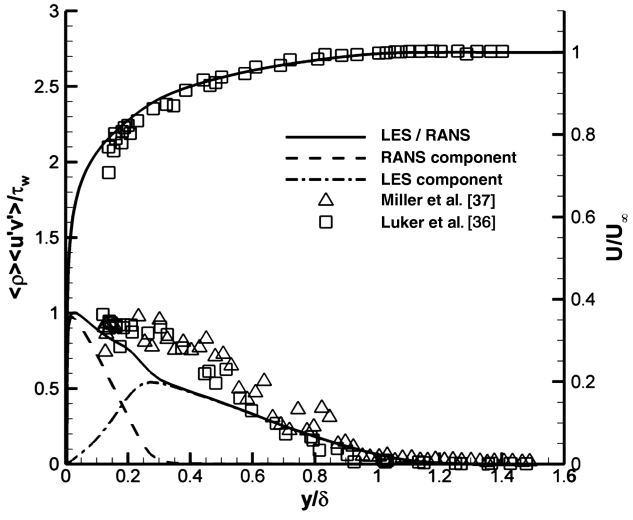

Fig. 2 Velocity and shear-stress boundary-layer profiles upstream of injector.

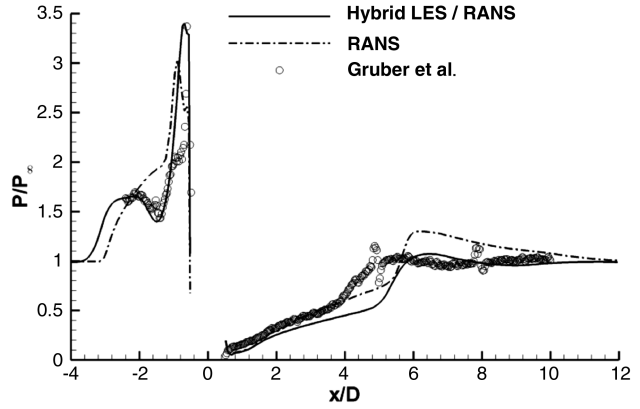

Fig. 3 Centerline surface pressure profile (sonic air injection, Gruber et al. experiments [10–13]).

B. Case 1: Sonic Air Injection

Figure 3 compares the centerline pressure distribution obtained from the hybrid LES/RANS model with the experimental data of Gruber et al. [10] and with a distribution obtained from the Menter-BSL RANS model. The LES/RANS model accurately predicts the pressure distribution upstream of the injector position but overpredicts the pressure level in the wake region downstream of the injector. Relative to the experimental measurements, both models predict a delayed recovery of the pressure downstream of the injector. The pressure peak in this region is better predicted by the hybrid LES/RANS model. Transverse pressure distributions in Fig. 4 reveal good agreement with experimental data at locations upstream of the injector, indicating that the upstream extent of the separation region induced by the bow shock is captured correctly. Downstream of the injection location, both models underpredict the offcenter pressure profiles, while the RANS model overpredicts the pressure peaks at the centerline for the last three stations. The slight asymmetry in the LES/RANS profiles suggests a lack of complete statistical convergence.

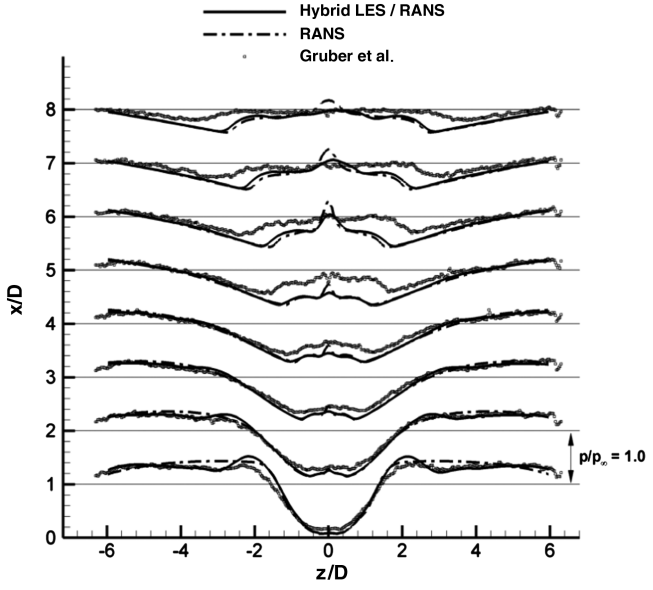

Fig. 4 Transverse surface pressure profiles (sonic air injection, Gruber et al. experiments [10–13]).

Figure 5 shows snapshots of inlet-air species density at the x-y centerplane and at a crossflow station located at $x/D = 5.9$. An intense near-field mixing process, characterized by a dominant pair of counter-rotating streamwise-oriented vortices and shear-layer Kelvin–Helmholtz structures, is illustrated in the density contours. Time-averaged inlet-air density contours at the x-y centerplane are compared with Mie-scattering data provided by Gruber et al. [10] in Fig. 6. Good agreement is generally indicated. Figure 7c shows the time-averaged mass fraction at the x-y centerplane, with the x and y coordinates normalized by the product of the momentum-flux ratio ($J = 2.90$) and the injector diameter. The results are compared with a penetration curve [12] determined experimentally from the averaged Mie-scattering data by mapping the 90% intensity contour, determined relative to an arbitrary value behind the bow shock. The penetration curve [which is valid up to $\sim(x + r)/(J^*D) = 1.5$] bisects the outer edge of the jet shear layer. Figures 7a and 7b compare the inlet-air density standard deviation with the experimental intensity standard deviation (normalized to lie between zero and one). The density standard deviations were determined over a sample space of only 50 frames, which is comparable to the experimental sample space of 100 frames. The results are thus not as smooth as those shown in Figs. 6 and 7c, which were obtained by averaging over $\sim$24, 000 frames. Figures 7b and 7c indicate close agreement with the structural features shown in the experiment, but it is clear that the jet penetration is slightly overpredicted.

Comparisons of time-averaged inlet-air density with experimental Mie-scattering images at $x/D = 0$, $x/D = 4$, $x/D = 8$, and $x/D = 10$ are shown in Fig. 8. The result from the LES/RANS model shows relatively good agreement with the positions of the jet plume at each station. The bow shock at the first station is also distinct, and its shape is consistent with the experimental data. The RANS solution shows very different plume shapes that display more distinct vortical features, as well as sharp transitions between the jet and inlet airstreams. Considering the differences in the numbers of frames

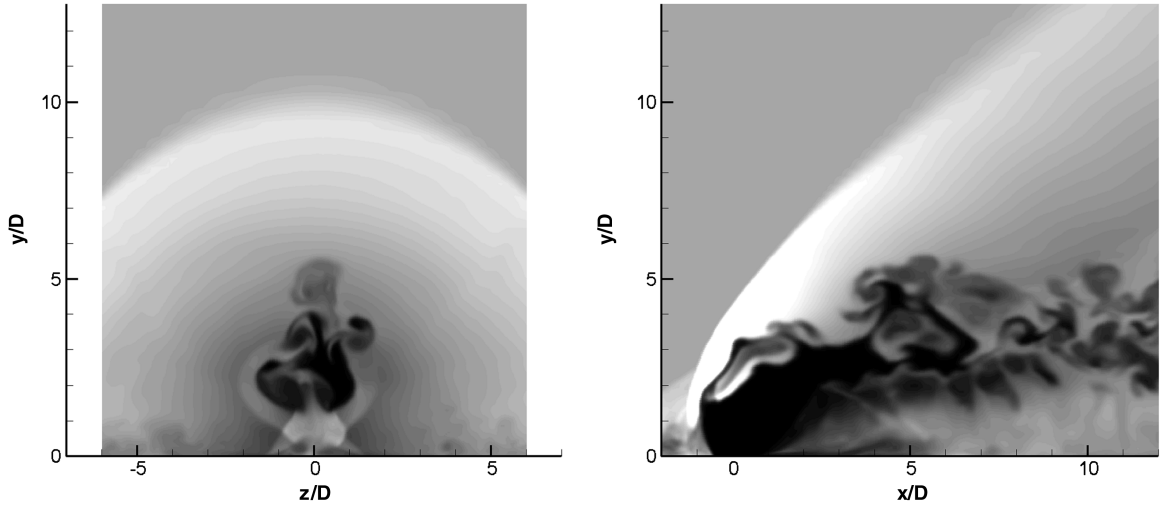

Fig. 5 Species density snapshots for air injection: LES/RANS (Gruber et al. experiments [10–13]).

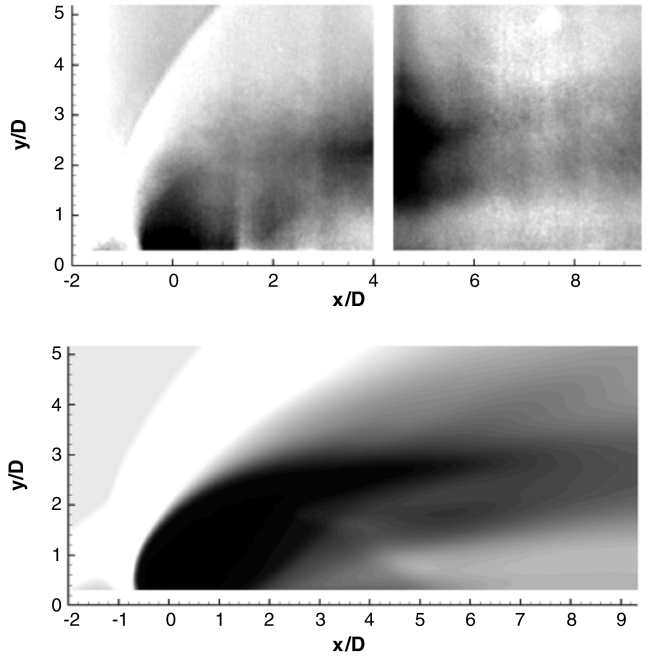

Fig. 6 Centerplane Mie-scattering images (top) and time-averaged species density contours (bottom) for air injection (Gruber et al. experiments [10–13]).

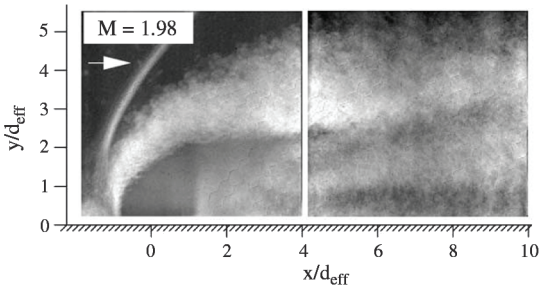

a) Intensity standard deviation [12]

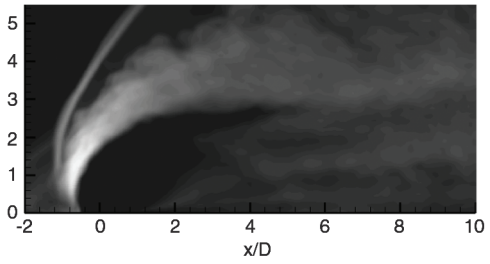

b) Standard deviation of inlet air density, LES/RANS

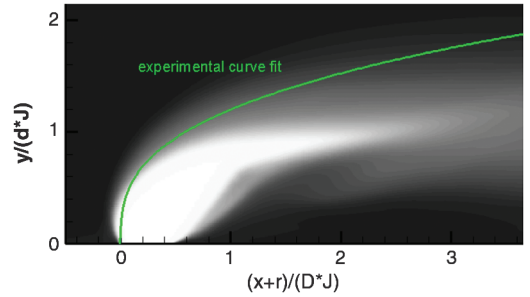

c) Time-averaged mass fraction, LES/RANS

Fig. 7 Centerplane time-averaged mass fraction and density standard deviation comparisons for sonic air injection (Gruber et al. experiments [10–13]).

used in the averaging (∼24, 000 in the calculations versus 50 or 100 in the experiments) and in the use of arbitrary intensities in normalizing the Mie-scattering images, it is difficult to compare the darkening/lightening of the contours in any quantitative sense. Visually though, it appears that the plumes in the experiment are more elongated in the transverse direction and tend to narrow in the spanwise (lateral) direction as one proceeds downstream. In contrast, the computed plumes appear to expand in a more uniform manner in the y and z directions. This may be an indication of the effects of flow confinement in the experiment.

C. Case 2: Sonic Helium Injection

Figure 9 shows instantaneous snapshots of inlet-air density for the case of sonic injection of helium into an air crossflow (Table 2). In comparison with Fig. 5, one can note darker contours within the plume, indicating less large-scale entrainment of the airstream into the jet fluid. The eddy sizes appear to be slightly smaller for the helium injection than in the air injection case. Time-dependent animations for both air and helium injection show that the dynamics of the shock system influence the initial growth of Kelvin–Helmholtz structures in the outer part of the jet shear layer. These structures break down more quickly for the helium injection case. Time-averaged mass fraction distributions and standard deviation comparisons are shown in Fig. 10. The experimental penetration curve lies closer to the outer edge of the jet than in the air injection case (Fig. 10c), and visual comparisons of Figs. 10a and 10b indicate good agreement with the structural features of the jet. The jet penetration appears to be better predicted for the helium injection case than for the air injection case (Fig. 6). Figure 11, however, shows several discrepancies in the cross-plane structure of the plume. The simulation predicts a wider plume at $x/D = 8$ and $x/D = 10$, with the bottom edges of the counter-rotating vortex pairs located further from the bottom wall than indicated in the Mie-scattering data. In contrast, the counter-rotating vortex pair is less well defined in the predictions at $x/D = 8$, relative to the experimental image.

D. Case 3: Sonic Ethylene Injection

The hybrid LES/RANS model has also used to simulate sonic injection of ethylene into Mach 1.98 air (Table 3). The snapshots of the inlet-air density in Fig. 12 show much less transverse penetration of the jet, compared with the air and helium cases. This is due to the fact that the momentum-flux ratio for the ethylene injection case is 0.50 compared with approximately 2.9 for the air and helium injection cases. For this case, Lin et al. [14] used the Raman-scattering technique to provide quantitative measurements of species densities of nitrogen, oxygen and ethylene. The Raman-scattering data can be translated into a mixture fraction, as seen in Fig. 13. Aside from a higher concentration of ethylene in the core of the plume at $x/D = 5$, the LES/RANS model accurately predicts the concentration and structure of the time-averaged ethylene plume. The lines delineating the stoichiometric mixture fraction for the experimental and numerical simulation agree very well. The widths of the plumes in Fig. 13 also agree well, although the plumes computed using the LES/RANS model are skewed slightly to the right due to a lack of complete statistical convergence. Also shown in Fig. 13 are results obtained using the Menter-BSL RANS model. The counter-rotating vortical structures are more pronounced, and the overall rate of mixing of the injectant with the air is reduced significantly, compared with the LES/RANS predictions and the experimental data. It should be noted that recent predictions of this flow, using RANS turbulence models that account for Schmidt and Prandtl number variation [20,21], are in better agreement with experimental data than the RANS results shown here.

E. Jet Penetration Comparisons

Transverse and spanwise injectant penetration values for the air and helium injection cases are compared with the data of Gruber et al. [10,12] in Fig. 14. Computational transverse penetration values at a particular x/D station are found by determining the location of the

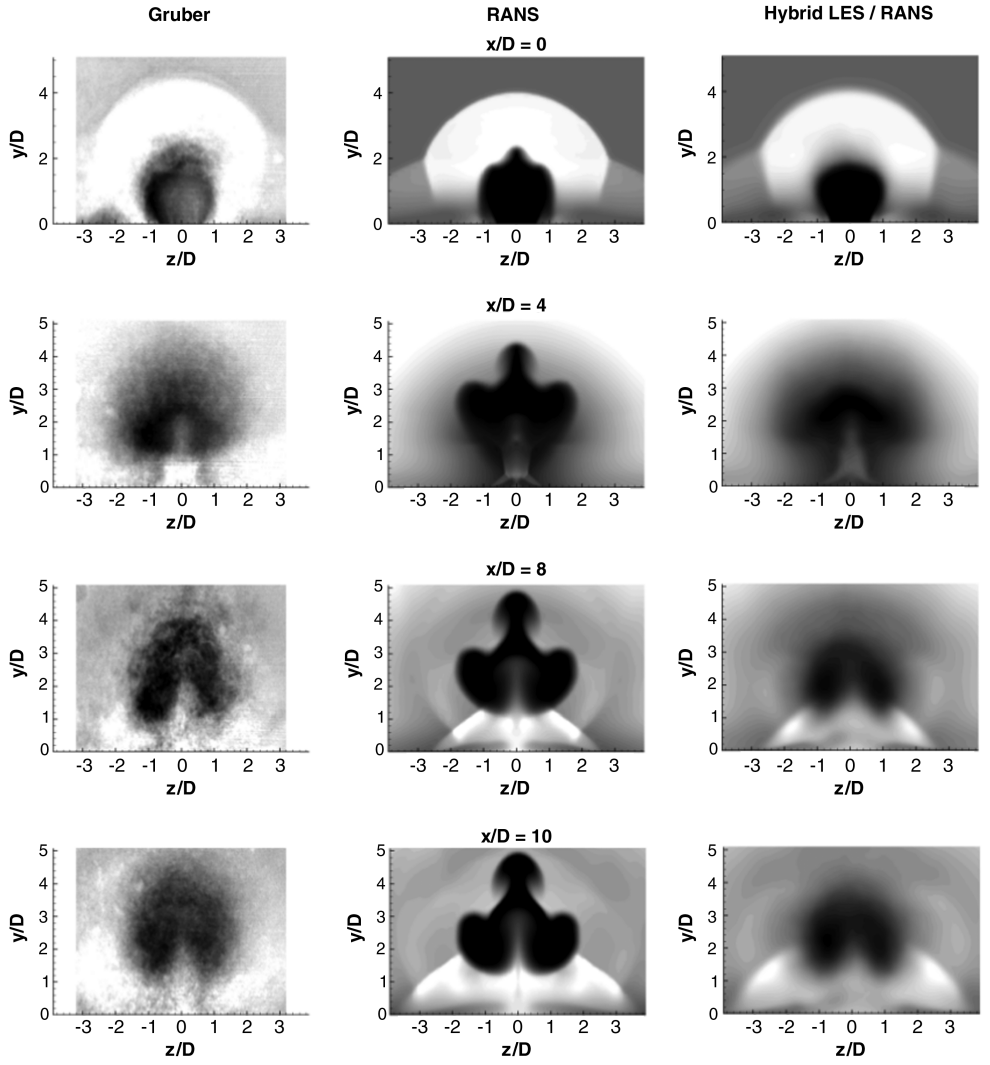

Fig. 8 Transverse experimental Mie-scattering images and computational contours of species density for sonic injection of air (Gruber et al. experiments [10–13]).

90% injectant mass fraction contour at its outermost point. The transverse penetration profiles (Fig. 14a) show that the locations of the tops of the plumes are predicted fairly well for the air case at $x/D = 0$ and $x/D = 4$, even though the visual comparisons of Fig. 7 suggest more penetration in the calculations. The transverse penetration for the air injection case is slightly overpredicted by the computational simulation and the helium transverse penetration is slightly underpredicted. For the air penetration case, the Gruber et al. data shows no increase in transverse penetration at $x/D = 8$ or $x/D = 10$. The computational simulation shows a slight increase in penetration between $x/D = 4$ and $x/D = 8$, which results in an 18% overprediction of penetration at that station and the next. For the

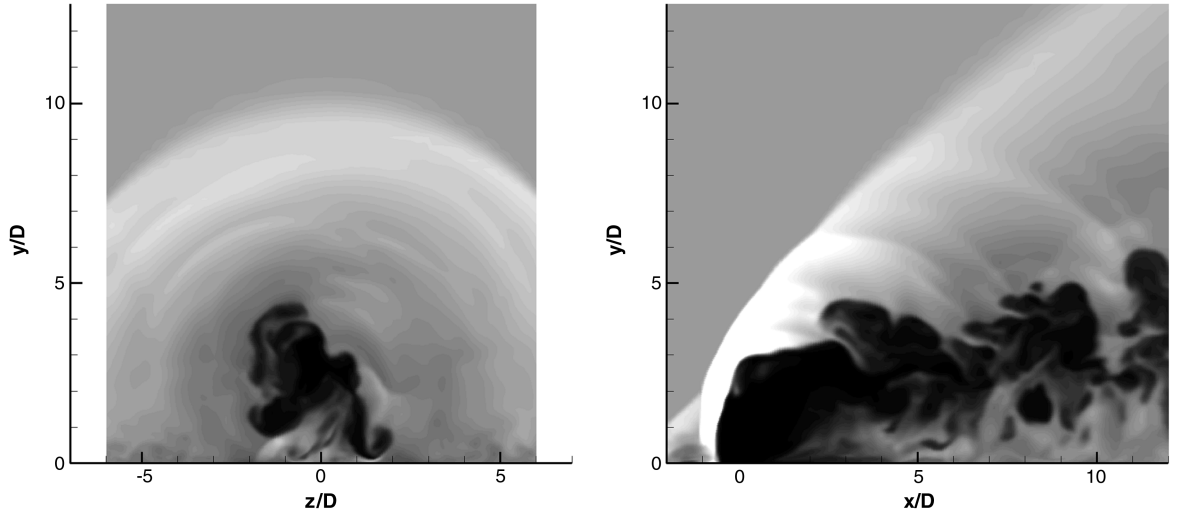

Fig. 9 Species density snapshots for helium injection: LES/RANS (Gruber et al. experiments [10–13]).

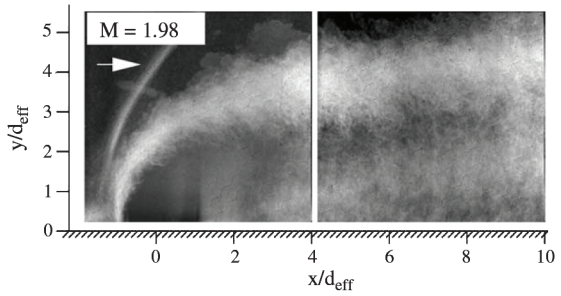

a) Intensity standard deviation [12]

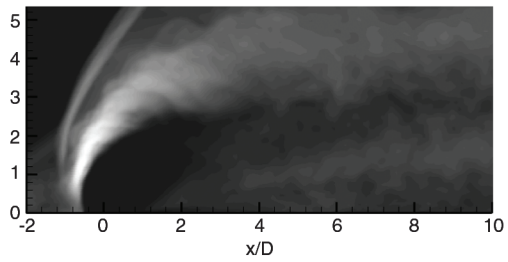

b) Standard deviation of inlet helium density, LES/RANS

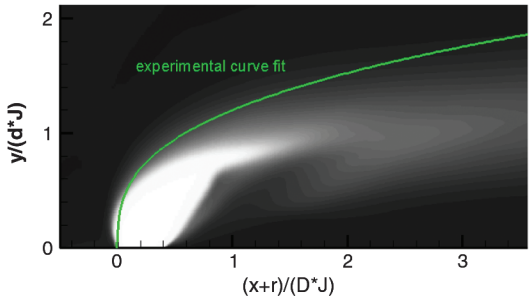

c) Time-averaged mass fraction, LES/RANS

Fig. 10 Centerplane time-averaged mass fraction and density standard deviation comparisons for sonic helium injection (Gruber et al. experiments [10–13]).

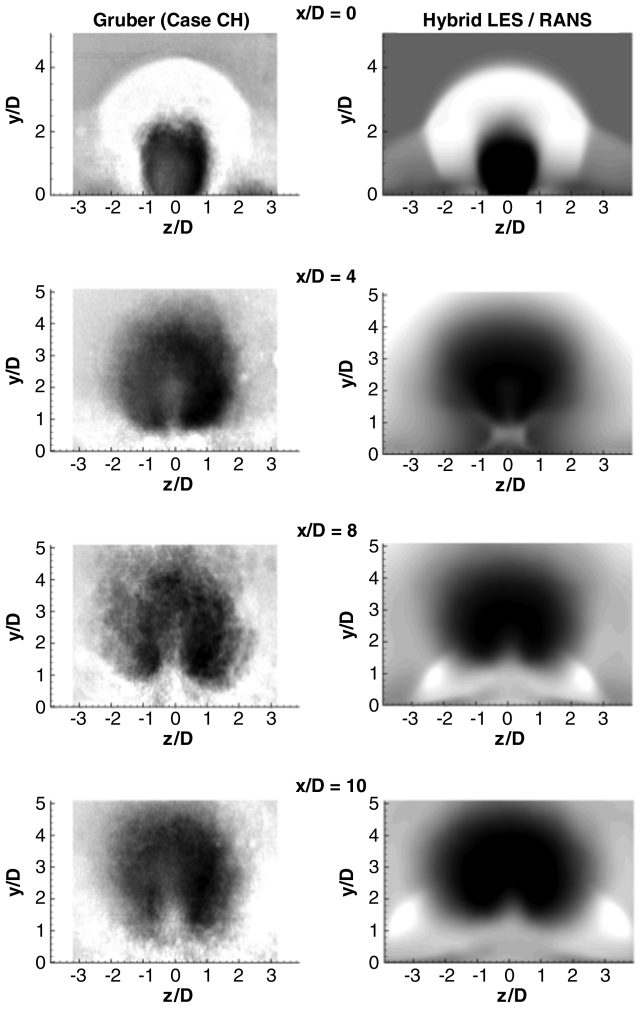

Fig. 11 Transverse experimental Mie-scattering images and computational contours of species density for sonic injection of helium. (Gruber et al. experiments [10–13]).

helium injection, the computational and experimental plots show similar trends in the first three stations (with the experimental penetration slightly higher than the computational predictions). At the final station, the experimental data shows a decrease in penetration, and the hybrid LES/RANS simulation predicts a slight increase in penetration, which results in a near-exact match between the computational and experimental results, despite the difference in the trend.

Spanwise penetration is a measurement of the maximum span of the plume (again determined by the 90% injectant mass fraction contour) normalized by the injector nozzle diameter. For the air injection case, the spanwise penetration (Fig. 14b) is similar to the experimental data for the first two stations, but the downward trend of the spanwise penetration indicated in the experimental data at the last two stations is not seen in the calculations. This corresponds to the narrowing of the plume indicated in the Mie-scattering images (Fig. 8), which is not predicted by the simulations. Palekar et al. [17] saw a similar discrepancy in their predictions of spanwise penetration for this experiment. The experimental spanwise penetration data for the helium plume does not show a substantial decrease at the last two stations, even though the images do indicate some elongation of the plume in the transverse direction. The calculation matches the lateral expansion rate of the helium plume but, again, underpredicts the measured values.

Experimental measurements of ethylene jet penetration (Fig. 15) show that the computational predictions closely match the experimental measurements, while the Lin et al. correlation slightly underpredicts penetration downstream. Lin et al. [14] also used the JETPEN code of Billig and Schetz [38] to predict penetration. The JETPEN prediction is near to those in the current work and the experimental data until about $(x + r)/D = 12$, where it starts to underpredict the plume's upper boundary. Lin et al. [14] note that the JETPEN code was calibrated for momentum-flux ratios of 1.0 to 10.0, whereas this case has a momentum-flux ratio of 0.5.

F. Calculation of Turbulent Schmidt Number

A significant source of uncertainty in RANS calculations of high-speed engine flowfields is the specification of the turbulent Prandtl and Schmidt numbers. These scale the turbulent heat conduction and diffusion terms, which are typically modeled using gradient-diffusion assumptions. Several studies ([39], for example) have shown the extreme sensitivity of RANS calculations to the choices of the turbulent Prandtl and Schmidt numbers. While models exist to calculate the variation of these quantities as part of a RANS solution [20–22,40,41], their development has been hampered by the lack of detailed experimental data for the turbulent scalar fluxes. One of the advantages of an LES approach is that larger-scale transport mechanisms are directly captured and, given an LES (or hybrid LES/RANS) database, it is possible to extract Favre-averaged distributions of fluxes of mass, momentum, and energy (due to turbulent fluctuations) and to compare them with Boussinesq/gradient-diffusion closures commonly used in RANS modeling. It should be noted that, while constant Schmidt and Prandtl numbers are assumed in the present LES/RANS model, the effects of this assumption are confined to the first 15 to 25% of the boundary layer (the region of the flow primarily modeled as unsteady RANS) and to the subgrid-scale modeling of scalar transport. Fluctuations in the scalar fluxes due to

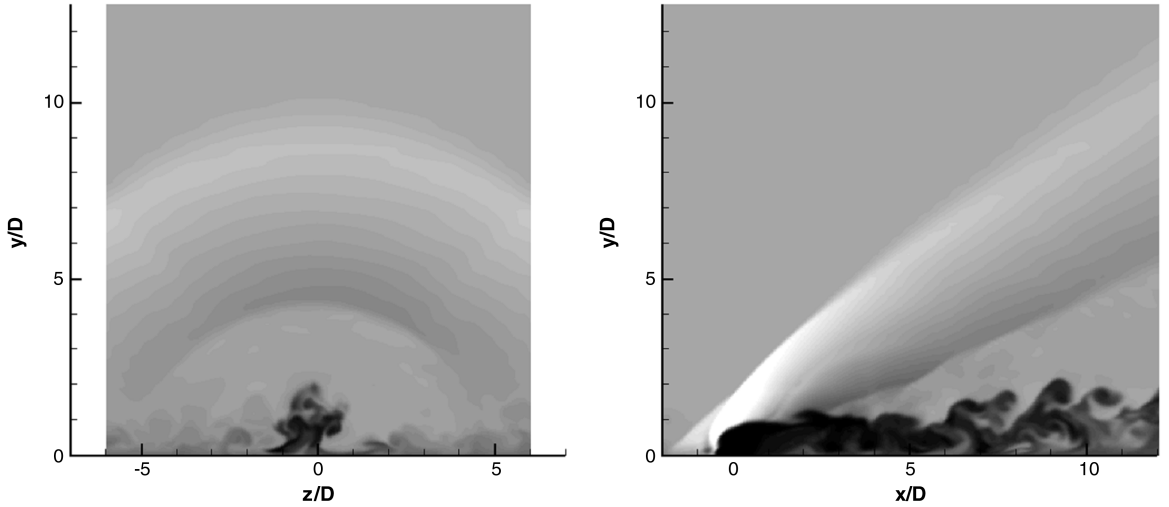

Fig. 12 Species density snapshots for sonic ethylene injection: LES/RANS (Lin et al. [14] experiments).

resolved-scale eddy motion are captured directly in the LES/RANS simulations, and we wish to examine whether or not the time-averaged effects of these fluctuations can be characterized by gradient-diffusion assumptions with a constant Schmidt number.

A flux of a variable $\phi' = [Y', u_i', T']$ may be expressed as

$$\overline{\rho u_j' \phi'} = \overline{\rho u_j \phi} - \frac{\overline{\rho u_j}\,\overline{\rho \phi}}{\bar{\rho}} \tag{5}$$

where the overbars indicate time averages. For turbulent mass transport, the value above may be correlated with a gradient-diffusion parameterization:

$$\overline{\rho u_j' Y'} = -\bar{\rho} \nu_{t,\text{mass},j} \frac{\partial \tilde{Y}}{\partial x_j} \tag{6}$$

where a Favre-averaged variable $\tilde{\phi}$ ($\phi = [Y, u_i, T]$) is defined as $\tilde{\phi} = \overline{\rho\phi}/\rho$. In general, separate eddy viscosities $\nu_{t,\text{mass},j}$ could be determined for each component of the gradient vector. The validity of the gradient-diffusion assumption requires that $\overline{\rho u_j' Y'}$ be well correlated with the gradient in mass fraction. We have verified that this is case for the mixing region downstream of the injection, at least for the y and z directions [42]. As RANS models will typically use an isotropic eddy viscosity, Eq. (6) can be rewritten as $\overline{\rho u_j' Y'} = -\bar{\rho} \nu_{t,\text{mass}} (\partial \tilde{Y}/\partial x_j)$, and an effective isotropic eddy viscosity associated with mass transport can be determined by taking an L_2 norm of the turbulent diffusion velocity vector:

$$\nu_{t,\text{mass}} \approx -\frac{\langle \overline{\rho u_i' Y'} (\partial \tilde{Y}/\partial x_i) \rangle}{\langle \bar{\rho} (\partial \tilde{Y}/\partial x_i)(\partial \tilde{Y}/\partial x_i) \rangle} \tag{7}$$

Here, the outer brackets denote a spatial filtering operation used to reduce statistical fluctuations. Similarly, one can define isotropic eddy viscosity associated with momentum transport as follows:

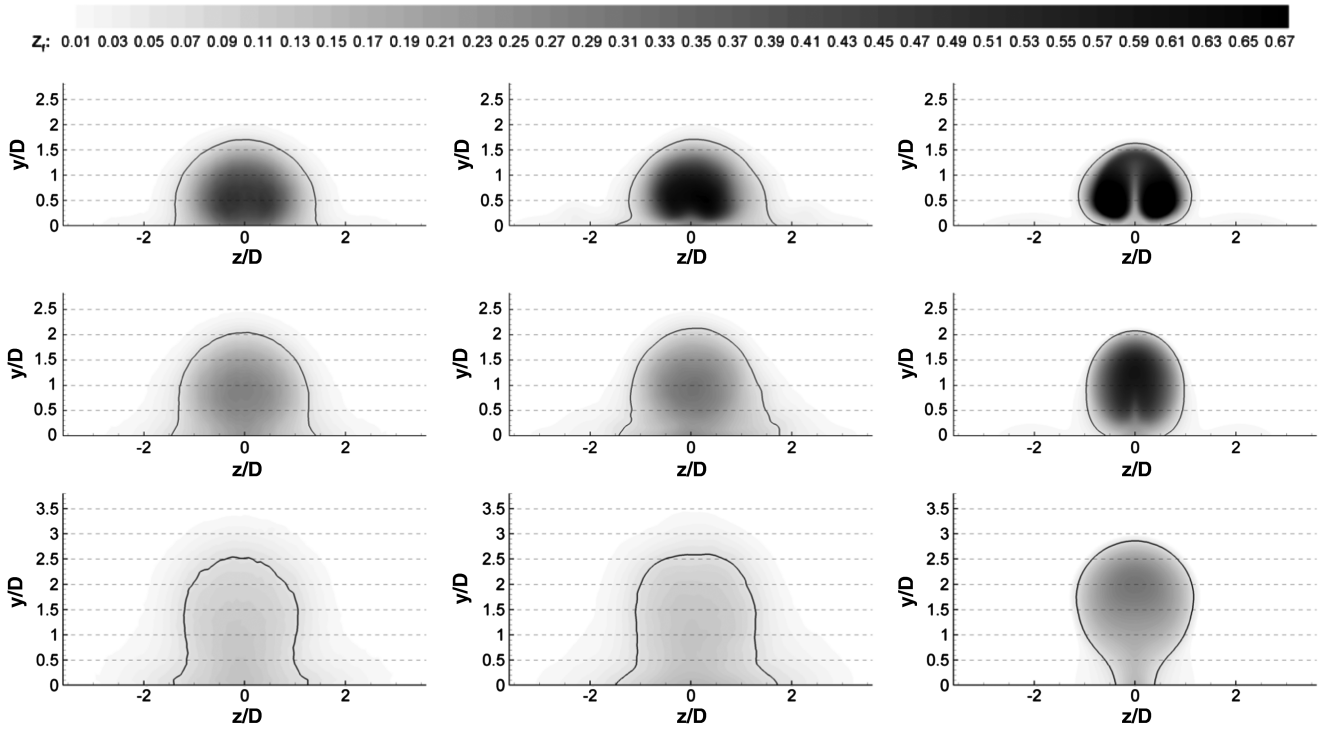

a) Raman scattering **b) LES / RANS** **c) RANS**

Fig. 13 Comparison of mixture fraction contours at different stations downstream of the injection port (top: $x/D = 5$, middle: $x/D = 10$, bottom $x/D = 25.3$). Solid line indicates stoichiometric mixture fraction of 0.0636 (Lin et al. [14] experiments).

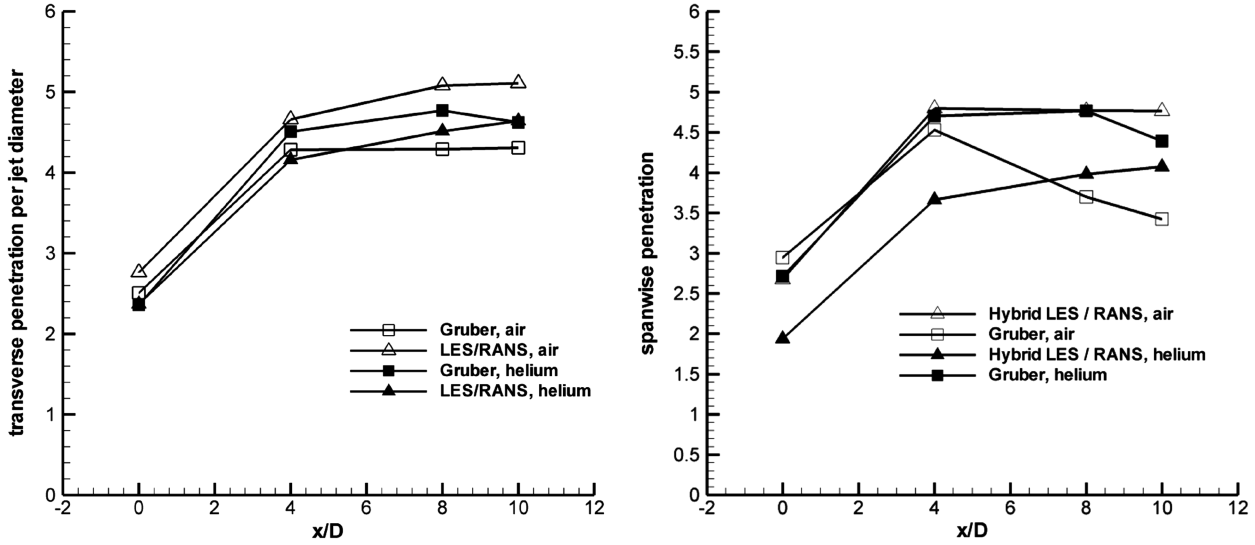

Fig. 14 Penetration profiles: transverse (left) and spanwise (right) (Gruber et al. experiments [10–13]).

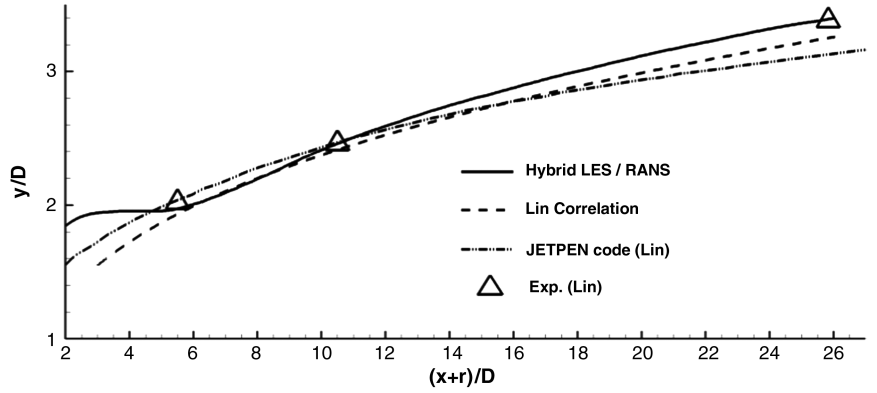

Fig. 15 Penetration comparison for ethylene injection (99% mixture fraction, Lin et al. [14] experiments).

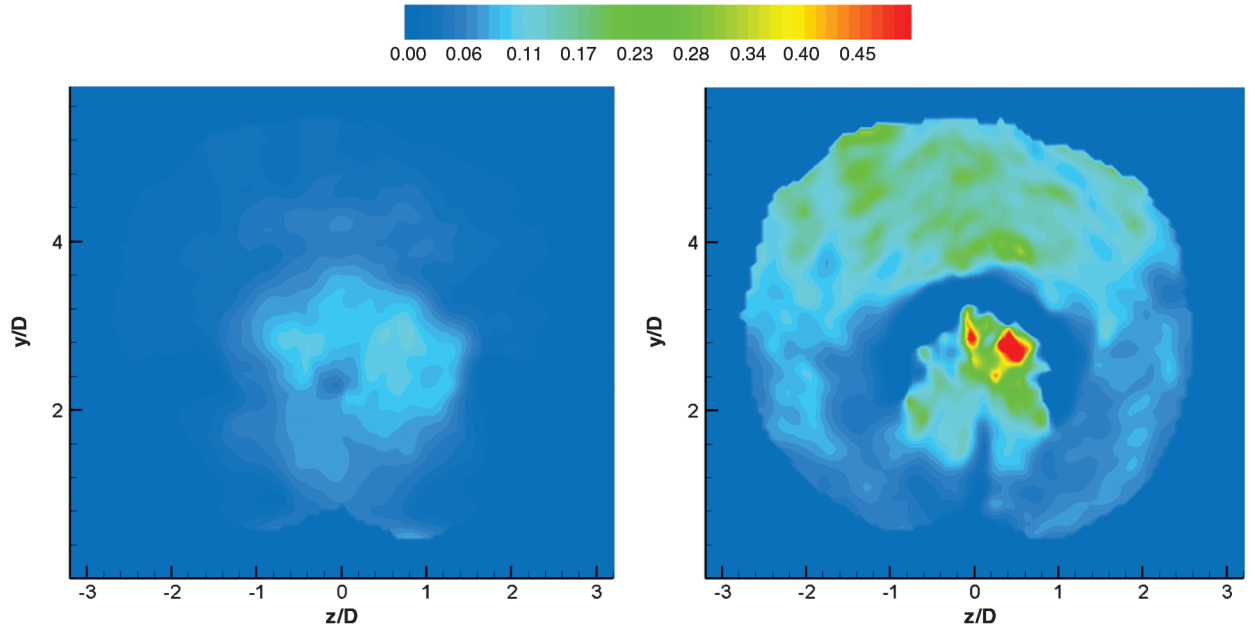

a) Momentum b) Mass

Fig. 16 Contours of effective eddy viscosities for momentum and mass for sonic air injection ($x/D = 10.9$; Gruber et al. experiments [10–13]).

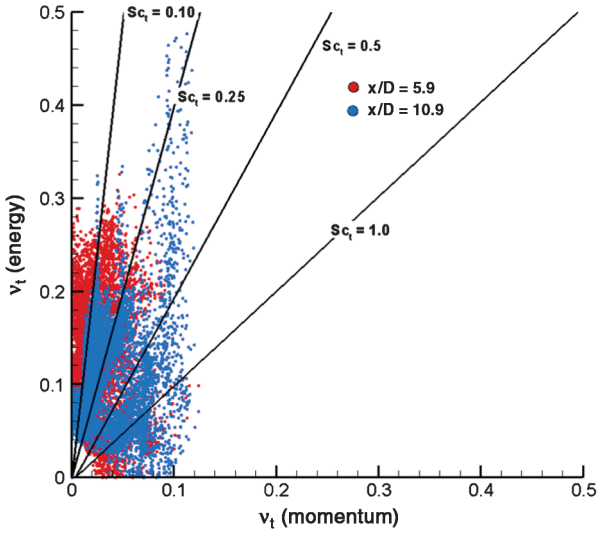

Fig. 17 Scatter plot of momentum eddy viscosity versus mass eddy viscosity (air injection, Gruber et al. experiments [10–13]).

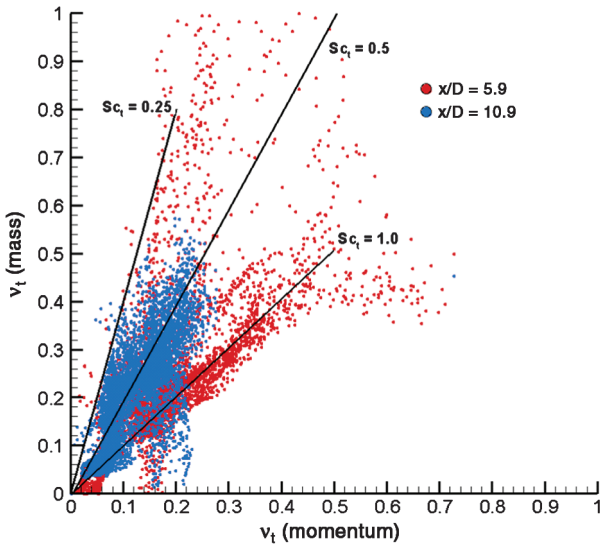

Fig. 19 Scatter plot of momentum eddy viscosity versus mass eddy viscosity (helium injection, Gruber et al. experiments [10–13]).

$$\nu_{t,\mathrm{mom}} \approx -\frac{\langle(\overline{\rho u_i' u_j'} - [(2/3)\delta_{ij}\overline{\rho k}]S_{ij}(\tilde{u}_i)\rangle}{\langle\bar{\rho}S_{ij}(\tilde{u}_i)S_{ij}(\tilde{u}_i)\rangle}$$

$$S_{ij}(\tilde{u}_i) = \frac{\partial\tilde{u}_i}{\partial\tilde{u}_j} + \frac{\partial\tilde{u}_j}{\partial\tilde{u}_i} - \frac{2}{3}\frac{\partial\tilde{u}_k}{\partial\tilde{u}_k}; \qquad \overline{\rho k} = \frac{1}{2}\left(\overline{\rho u_k u_k} - \frac{\overline{\rho u_k}\,\overline{\rho u_k}}{\bar{\rho}}\right) \quad (8)$$

Turbulent Schmidt numbers may then be calculated by taking ratios of these isotropic eddy viscosities:

$$\frac{1}{Sc_t} = \frac{\nu_{t,\mathrm{mass}}}{\nu_{t,\mathrm{mom}}} \quad (9)$$

Similar procedures can be used to estimate the turbulent Prandtl number. In general, this calculation requires statistics for temperature–species correlations, as well as consideration of specific heat variations with temperature. Preliminary results were reported in [43] for the air injection case.

Figure 16 shows predictions of the isotropic eddy viscosities associated with turbulent momentum and mass transport for the air injection case at $x/D = 10.9$. The calculation extent is restricted to the area bounded by the 95% inlet-air mass fraction contour. There is some similarity between the momentum and energy eddy-viscosity distributions, but the mass eddy-viscosity distribution shows large values near the outer region of the plume that do not appear to be highly correlated with momentum transport in this region. A scatter plot of mass eddy viscosity versus momentum eddy viscosity is shown in Fig. 17. A constant Schmidt number parameterization would result in the collapse of the data band around a line of constant slope (several such lines are indicated in the figure). The shape of the scatter plots indicates that the average Schmidt number is very low (of the order of 1/10 or less) at both $x/D = 5.9$ and $x/D = 10.9$. Significant deviations from this average are present, particularly in the outer regions of the plume. For this case, the average momen tum eddy viscosity (m^2/s) over the plume cross section is 0.0196 at $x/D = 0.0$, 0.0226 at $x/D = 5.9$, and 0.0426 at $x/D = 10.9$. Normalized with respect to the incoming air kinematic viscosity of $1.34e-5$ m^2/s, these values become 1463 at $x/D = 0.0$, 1686 at $x/D = 5.9$, and 3179 at $x/D = 10.9$. These values are similar to those provided by RANS turbulence models for free-shear layers at high Reynolds numbers.

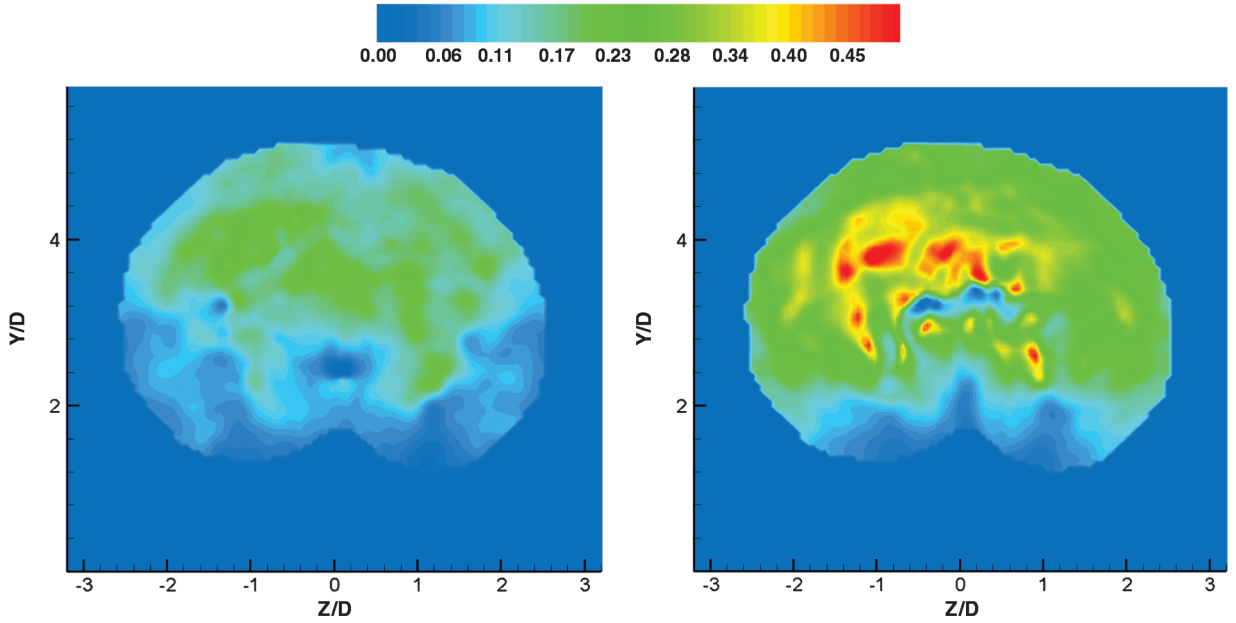

a) Momentum **b) Mass**

Fig. 18 Contours of effective eddy viscosities for momentum and mass for helium injection ($x/D = 10.9$, Gruber et al. experiments [10–13]).

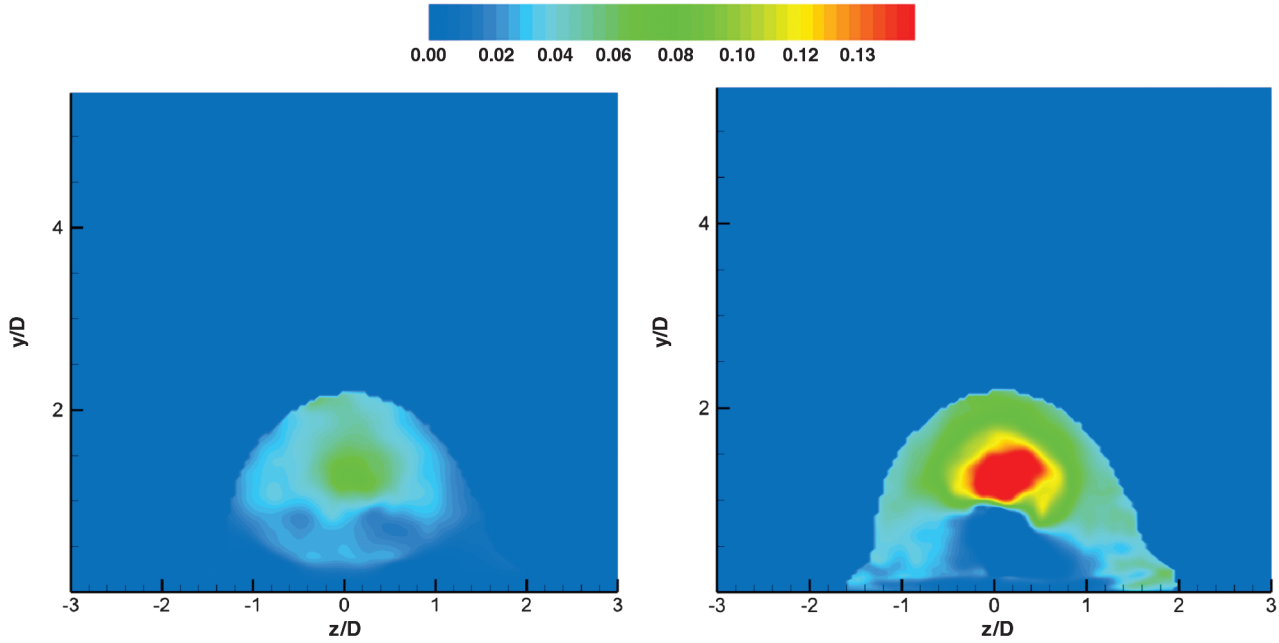

a) Momentum b) Mass

Fig. 20 Contours of effective eddy viscosities for momentum and mass for sonic ethylene injection ($x/D = 10$, Lin et al. [14] experiments).

Figure 18 indicates more similarity among the momentum and mass eddy viscosities for the helium case at $x/D = 10.9$. The mass and momentum eddy viscosities are in closer agreement. The average momentum eddy viscosities (m^2/s) are higher than in the air injection case: 0.0532 (normalized: 3941) at $x/D = 0.0$, 0.200 (normalized: 14,925) at $x/D = 5.9$, and 0.132 (normalized: 9892) at $x/D = 10.9$. In a RANS context, these differences appear to be associated with the larger velocity difference between the streams and imply more turbulence production associated with stronger velocity gradients. The scatter plot in Fig. 19 indicates that the mass and momentum eddy viscosities start to collapse toward the line associated with a Schmidt number of approximately 0.5 at the $x/D = 10.9$ station. At the $x/D = 5.9$ station, a bimodal behavior is indicated, with some data arranged about the $Sc_t = 1.0$ line and the rest oriented about the $Sc_t = 0.5$ line. For low molecular-weight fluids, a value of $Sc_t = 0.5$ is commonly adopted in RANS calculations, and it is noteworthy that the LES/RANS database predicts a collapse around this value at the most downstream station. The helium case appears to be less dominated by large-scale entrainment effects (macromixing) than the air case, and the fact that mixing appears to be occurring at a smaller scale may lead to a faster equilibration of the rates of mass and momentum transport.

Contours of momentum eddy viscosity and mass eddy viscosity for ethylene injection at $x/D = 10$ are shown in Fig. 20. The contours show clear similarities, especially in the high eddy-viscosity area in the core of the plume. The average momentum eddy viscosities (m^2/s) are lower than the helium and air injection cases: 0.002977 (normalized: 222.2) at $x/D = 0.0$, 0.01246 (normalized: 930.1) at $x/D = 5.9$, and 0.01387 (normalized: 1035). These lower values are likely due to the much lower momentum-flux ratio for this case than the other two. The scatter plot in Fig. 21 shows mass versus momentum eddy viscosity at $x/D = 10$ and $x/D = 25.3$. There is an indication of a collapse in the data about turbulent Schmidt number values of 0.4 to 0.6 for some regions within the plume. These results, taken together, indicate that the constant Schmidt number assumption is inadequate in general and that better models for the actual scalar flux [Eq. (5)] would appear to be a necessity for improved mixing predictions using RANS models. These LES/RANS predictions, while illustrative, appear to contain too much statistical error (caused primarily by insufficient evolution times) to be of direct use in constructing such models, though Tomes et al. [21] report that LES data sets similar to these are being used to assess the performance of a variable Schmidt/Prandtl number model described in [41].

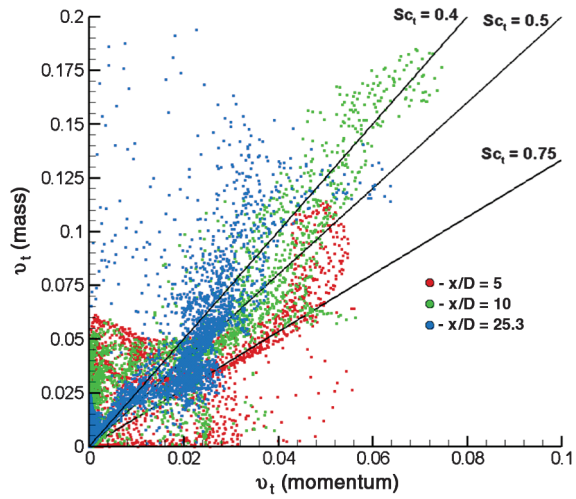

Fig. 21 Scatter plot of momentum eddy viscosity versus mass eddy viscosity (ethylene injection, Lin et al. [14] experiments).

IV. Conclusions

Hybrid LES/RANS simulations of sonic injection of air, helium, and ethylene into a nominal Mach 2 flow of air have been presented. The LES/RANS model shifts from RANS to LES through the action of a flow-dependent blending function, which is calibrated to induce the RANS to LES transition, where the boundary-layer structure changes from logarithmic behavior to a wakelike behavior. The upstream boundary-layer structure is predicted to good accord by the LES/RANS model, although the resolved Reynolds stresses do not completely reach their zero-pressure-gradient equilibrium values. For air injection, the LES/RANS simulations accurately predict the centerline pressure profile upstream of the injector but do not capture the rate of recovery of the pressure distribution downstream of the injection point. Species density and density variance predictions for both air and helium injection agree qualitatively with the Mie-scattering images of Gruber et al. [10–13]; but some effects, such as a lateral narrowing of the plume as it moves downstream, are not

captured in the calculations. Aside from evidence of slower mixing at the plume core (evident at the first transverse station), mixture fraction predictions for ethylene injection agree very well with the Raman-scattering data of Lin et al. [14]. The results obtained using the LES/RANS model indicate an improvement over the Menter-BSL RANS results in almost all areas. The penetration of the jet into the crossflow is slightly underpredicted for the helium injection case and is slightly overpredicted for the air injection case. Some of the possible reasons for the discrepancies between predictions and experiment for the air and helium injection cases include the differences in sample size for the time averages ($\sim$24, 000 images for the calculations, versus 50–100 for the experiment), inadequate resolution of the jet boundary layer as it enters the domain, and the assumption of negligible sidewall/upper wall influences in the calculations. The penetration of ethylene into the crossflow is very well predicted. An analysis of the LES/RANS results indicates that, for near-field mixing dominated by large-scale entrainment events, the assumption of constant Schmidt number is inadequate. As the eddies break down and the mixing occurs at smaller scales, the LES/RANS data indicates an equilibration of mass and momentum transport rates, characterized by an approximately constant value of the Schmidt number, might occur.

Acknowledgments

This work is supported by NASA under cooperative agreement NNX07AC27A-S01. Computer resources have been provided by the NASA Advanced Supercomputing division. The authors are grateful to Steven Lin of Taitech, Inc. and Campbell Carter of the U.S. Air Force Research Laboratory for providing experimental results and other information relating to their work.

References

[1] Hersch, M., Povinelli, L. A., and Povinelli, F. P., "Optical Study of Sonic and Supersonic Jet Penetration from a Flat Plate into a Mach 2 Airstream," NASA TN D-5717, March 1970.

[2] Schetz, J. A., "Interaction Shock for Transverse Injection in Supersonic Flow," *Journal of Spacecraft and Rockets*, Vol. 7, No. 2, Feb. 1970, pp. 143–149.
doi:10.2514/3.29889

[3] Schetz, J. A., Hawkins, P. F., and Lehman, H., "Structure of Highly Underexpanded Transverse Jets in a Supersonic Stream," *AIAA Journal*, Vol. 5, No. 5, May 1967, pp. 882–884.
doi:10.2514/3.4095

[4] Zukoski, E. E., and Spaid, F. W., "Secondary Injection of Gases into a Supersonic Flow," *AIAA Journal*, Vol. 2, No. 10, Oct. 1964, pp. 1689–1696.
doi:10.2514/3.2653

[5] Schetz, J. A., and Billig, F. S., "Penetration of Gaseous Jets into a Supersonic Stream," *Journal of Spacecraft and Rockets*, Vol. 3, No. 11, Nov. 1966, pp. 1658–1665.
doi:10.2514/3.28721

[6] Andrepoulos, J., and Rodi, W., "Experimental Investigations of Jets in a Crossflow," *Journal of Fluid Mechanics*, Vol. 138, 1984, pp. 93–127.
doi:10.1017/S0022112084000057

[7] Wang, K. S., Smith, O. I., and Karagozian, A. R., "In Flight Imaging of Gas Jet Injected into Subsonic and Supersonic Crossflows," *AIAA Journal*, Vol. 33, No. 12, 1995, pp. 2259–2263.
doi:10.2514/3.12977

[8] McDaniel, J. C., and Graves, J., "Laser-Induced Fluorescence Visualization of Transverse Gaseous Injection in a Nonreacting Supersonic Combustor," *Journal of Propulsion and Power*, Vol. 4, No. 6, Nov.–Dec. 1988, pp. 591–597.
doi:10.2514/3.23105

[9] Hollo, S. D., McDaniel, J. C., and Hartfield, R. J., Jr., "Quantitative Investigation of Compressible Mixing: Staged Transverse Injection into Mach 2 Flow," *AIAA Journal*, Vol. 32, No. 3, 1994, pp. 528–534.
doi:10.2514/3.12017

[10] Gruber, M. R., Nejad, A. S., and Dutton, J. C., "An Experimental Investigation of Transverse Injection from Circular and Elliptical Nozzles into a Supersonic Crossflow," Wright Lab. TR 96-2102, Wright-Patterson AFB, OH, Jan. 1996.

[11] Gruber, M. R., Nejad, A. S., Chen, T. H., and Dutton, J. C., "Mixing and Penetration Studies of Sonic Jets in a Mach 2 Freestream," *Journal of Propulsion and Power*, Vol. 11, No. 2, March–April 1995, pp. 315–323.
doi:10.2514/3.51427

[12] Gruber, M. R., Nejad, A. S., Chen, T. H., and Dutton, J. C., "Compressibility Effects in Supersonic Transverse Injection Flowfields," *Physics of Fluids*, Vol. 9, No. 5, May 1997, pp. 1448–1461.
doi:10.1063/1.869257

[13] Gruber, M. R., Nejad, A. S., Chen, T. H., and Dutton, J. C., "Transverse Injection from Circular and Elliptical Nozzles into a Supersonic Crossflow," *Journal of Propulsion and Power*, Vol. 16, No. 3, May–June 2000, pp. 449–457.
doi:10.2514/2.5609

[14] Lin, K., Ryan, M., Carter, C., Gruber, M., and Raffoul, C., "Scalability of Ethylene Gaseous Jets for Fueling Scramjet Combustors at Various Scales," AIAA Paper 2009-1423, 2009.

[15] Uenishi, K., Rogers, R. C., and Northram, G. B., "Numerical Predictions of a Rearward-Facing Step Flow in a Supersonic Combustor," *Journal of Propulsion and Power*, Vol. 5, No. 2, pp. 158–164.
doi:10.2514/3.23131, 1989.

[16] Tam, C., Baurle, R. A., and Gruber, M. R., "Numerical Study of Injection into a Supersonic Crossflow," AIAA Paper 99-2254, June 1999.

[17] Palekar, A., Truman, C. R., and Vorobieff, P., "Prediction of Transverse Injection of a Sonic Jet in Supersonic Crossflow," AIAA Paper 2005-5366, June 2005.

[18] Maddalena, L., Campioli, T. L., and Schetz, J. A., "Experimental and Computational Investigation of Light–Gas Injectors in Mach 4.0 Crossflow," *Journal of Propulsion and Power*, Vol. 22, No. 5, Sep.–Oct. 2006, pp. 1027–1038.
doi:10.2514/1.19141

[19] Manna, P., and Chakraborty, D., "Numerical Investigation of Transverse Sonic Injection in a Non-Reacting Supersonic Combustor," *Proceedings of the Institution of Mechanical Engineers, Part G (Journal of Aerospace Engineering)*, Vol. 219, No. 3, 2005, pp. 205–215.
doi:10.1243/095441005X30261

[20] Keistler, P. G., and Hassan, H. A., "Simulation of Supersonic Combustion Involving H_2/Air and C_2H_4/Air," AIAA Paper 2009-29, Jan. 2009.

[21] Tomes, J., Kannepalli, C., Calhoon, W. H., and Seiner, J. M., "Studies to Validate Scalar Fluctuation Modeling in High Speed Jet Interaction Flowfields," AIAA Paper 2009-1115, Jan. 2009.

[22] Ungewitter, R. J., Brinckman, K., and Dash, S. M., "Advanced Modeling of New Fuel/Air Mixing Data Sets for Scramjet Applications," AIAA Paper 2009-4940, Aug. 2009.

[23] Spalart, P. R., Jou, W.-H., Strelets, M., and Allmaras, S. R., "Comments on the Feasibility of LES for Wings and on a Hybrid RANS/LES Approach," *Advances in DNS/LES*, edited by C. Liu, and Z. Liu, Greyden Press, Dayton, OH, 1998, p. 137.

[24] Spalart, P. R., Deck, S., Shur, M. L., Squires, K. D., Strelets, M. Kh., and Travin, A., "A New Version of Detached-Eddy Simulation, Resistant to Ambiguous Grid Densities," *Theoretical and Computational Fluid Dynamics*, Vol. 20, No. 3, 2006, pp. 181–195.
doi:10.1007/s00162-006-0015-0

[25] Kawai, S., and Lele, S. K., "Mechanisms of Jet Mixing in a Supersonic Crossflow: A Study Using Large-Eddy Simulation," *Center for Turbulence Research, Annual Research Briefs*, Stanford Univ., Stanford, CA, 2007, pp. 353–365.

[26] Santiago, J. G., and Dutton, J. C., "Velocity Measurements of a Jet Injected into a Supersonic Crossflow" *Journal of Propulsion and Power*, Vol. 13, No. 2, pp. 264–273.
doi:10.2514/2.5158, 1997.

[27] Peterson, D. M., Subbareddy, P. K., and Candler, G. V., "DES Investigations of Transverse Injection into Supersonic Crossflow using a Hybrid Unstructured Solver," AIAA Paper 2006-0903, Jan. 2006.

[28] Higgins, K., and Schmidt, S., "Simulation of a Sonic Jet Injected into a Supersonic Cross-Flow," *16th Australasian Fluid Mechanics Conference*, Univ. of Queensland, Queensland, Australia, Dec. 2007, pp. 608–612.

[29] Edwards. J. R., Choi, J.-I., and Boles, J. A., "Hybrid LES/RANS Simulation of a Mach 5 Compression-Corner Interaction," *AIAA Journal*, Vol. 46, No. 4, 2008, pp. 977–991.
doi:10.2514/1.32240

[30] Choi, J.-I., Edwards, J. R., and Baurle, R. A., "Compressible Boundary Layer Predictions at High Reynolds Number Using Hybrid LES/RANS Methods," *AIAA Journal*, Vol. 47, No. 9, 2009, pp. 2179–2193.
doi:10.2514/1.41598

[31] Menter, F. R., "Two-Equation Eddy-Viscosity Turbulence Models for Engineering Applications," *AIAA Journal*, Vol. 32, No. 8, 1994, pp. 1598–1605.
doi:10.2514/3.12149
[32] Walz, A., *Boundary Layers of Flow and Temperature*, MIT Press, Cambridge, MA, 1969.
[33] Edwards, J. R., "A Low-Diffusion Flux-Splitting Scheme for Navier–Stokes Calculations," *Computers and Fluids*, Vol. 26, No. 6, 1997, pp. 635–659.
doi:10.1016/S0045-7930(97)00014-5
[34] Colella, P., and Woodward, P. R., "The Piecewise Parabolic Method (PPM) for Gas-Dynamical Simulations," *Journal of Computational Physics*, Vol. 54, No. 1, 1984, pp. 174–201.
doi:10.1016/0021-9991(84)90143-8
[35] Gruber, M. R., and Nejad, A. S., "New Supersonic Combustion Research Facility," *Journal of Propulsion and Power*, Vol. 11, No. 5, 1995, p. 1080.
doi:10.2514/3.23940
[36] Luker, J. J., Bowersox, R. D. W., and Buter, T. A., "Influence of Curvature-Driven Favorable Pressure Gradient on Supersonic Turbulent Boundary Layer," *AIAA Journal*, Vol. 38, No. 8, 2000, pp. 1351–1359.
doi:10.2514/2.1134
[37] Miller, R., Dotter, J., Bowersox, R. D. W., and Buter, T. A., "Compressible Turbulence Measurements in Supersonic Boundary Layers with Favorable and Adverse Pressure Gradients," *Transitional and Turbulent Compressible Flows*, edited by E. F. Spina, and C. Arakawa, Vol. 224, American Society of Mechanical Engineers, New York, 1995, pp. 193–200.
[38] Billig, F. S., and Schetz, J., "Analysis of Penetration and Mixing of Gas Jets in Supersonic Cross Flow," AIAA Paper 92-5061, Dec. 1992.
[39] Baurle, R. A., and Eklund, D. R., "Analysis of Dual Mode Hydrocarbon Scramjet Operation at Mach 4–6.5," *Journal of Propulsion and Power*, Vol. 18, No. 5, 2002, pp. 990–1002.
doi:10.2514/2.6047
[40] Xiao, X., Edwards, J. R., Hassan, H. A., and Cutler, A. D., "Variable Schmidt Number Formulation for Scramjet Applications," *AIAA Journal*, Vol. 44, No. 3, 2006, pp. 593–599.
doi:10.2514/1.15450
[41] Brinckman, K., Calhoon, W. H., and Dash, S. M., "Scalar Fluctuation Modeling for High-Speed Aeropropulsive Flows," *AIAA Journal*, Vol. 45, No. 5, 2007, pp. 1036–1046.
doi:10.2514/1.21075
[42] Boles, J. A., "Hybrid Large-Eddy Simulation/Reynolds Averaged Navier–Stokes Methods and Predictions for Various High-Speed Flows," Ph.D. Dissertation, North Carolina State Univ., Aug. 2009.
[43] Boles, J. A., and Edwards, J. R., "Hybrid LES/RANS Simulation of Normal Injection into a Supersonic Cross-Stream," AIAA Paper 2008-0622, Jan. 2008.

P. Givi
Associate Editor